DRAFT VERSION MAY 8, 2022
Typeset using LaTeX **twocolumn** style in AASTeX62

Early Time Light Curves of 18 Bright Type Ia Supernovae Observed with TESS

M. M. FAUSNAUGH,[1] P. J. VALLELY,[2] C. S. KOCHANEK,[2,3] B. J. SHAPPEE,[4] K. Z. STANEK,[2,3] M. A.TUCKER,[4] GEORGE R. RICKER,[1] ROLAND VANDERSPEK,[1] DAVID W. LATHAM,[5] S. SEAGER,[1,6,7] JOSHUA N. WINN,[8] JON M. JENKINS,[9] TANSU DAYLAN,[1,10] JOHN P. DOTY,[11] GÁBOR FŰRÉSZ,[1] ALAN M. LEVINE,[1] ROBERT MORRIS,[9,12] ANDRÁS PÁL,[13,1,14] LIZHOU SHA,[1] ERIC B. TING,[9] AND BILL WOHLER[9,12]

[1]*Department of Physics and Kavli Institute for Astrophysics and Space Research, Massachusetts Institute of Technology, Cambridge, MA 02139, USA*
[2]*Department of Astronomy, The Ohio State University, 140 West 18th Avenue, Columbus, OH 43210, USA*
[3]*Center for Cosmology and AstroParticle Physics, The Ohio State University, 191 W. Woodruff Ave., Columbus, OH 43210, USA*
[4]*Institute for Astronomy, University of Hawai'i, 2680 Woodlawn Drive, Honolulu, HI 96822, USA*
[5]*Center for Astrophysics | Harvard & Smithsonian, 60 Garden Street, Cambridge, MA 02138*
[6]*Department of Earth, Atmospheric, and Planetary Sciences, Massachusetts Institute of Technology, Cambridge, MA 02139, USA*
[7]*Department of Aeronautics and Astronautics, MIT, 77 Massachusetts Avenue, Cambridge, MA 02139, USA*
[8]*Department of Astrophysical Sciences, Princeton University, 4 Ivy Lane, Princeton, NJ 08544, USA*
[9]*NASA Ames Research Center, Moffett Field, CA, 94035, USA*
[10]*Kavli Fellow*
[11]*Noqsi Aerospace Ltd, 15 Blanchard Avenue, Billerica, MA 01821, USA*
[12]*SETI Institute, Mountain View, CA 94043, USA*
[13]*Konkoly Observatory, Research Centre for Astronomy and Earth Sciences, Hungarian Academy of Sciences, Konkoly Thege Miklós út 15-17, H-1121 Budapest, Hungary*
[14]*Department of Astronomy, Loránd Eőtvős University, Pázmány P. stny. 1/A, Budapest H-1117, Hungary*

ABSTRACT

We present early time light curves of 18 Type Ia supernovae observed in the first six sectors of TESS data. Nine of these supernovae were discovered by ASAS-SN, four by ATLAS, four by ZTF, and one by *Gaia*. For eight of these objects with sufficient dynamic range (>3.0 mag from detection to peak), we fit power law models and search for signatures of companion stars. Most of our sources are consistent with fireball models where the flux increases $\propto t^2$, while two display a flatter rise with flux $\propto t$. We do not find any obvious evidence for additional structure such as multiple power law components in the early rising light curves. Assuming a favorable viewing angle, we place conservative upper limits on the radii of any companion stars of $\lesssim 25\ R_\odot$ for six supernovae and $\lesssim 4\ R_\odot$ for 4 supernovae. If such systems are commonplace, the odds of non-detection in this sample are 38% for companions $\gtrsim 25\,R\odot$ and 52% for companions $\gtrsim 4\,R\odot$. Based on the examples in this work, we expect that TESS will either detect emission from a dwarf companion during its initial two year survey, or place stringent limits on single-degenerate progenitor models.

Keywords: supernovae:general

1. INTRODUCTION

A key observation for studying the progenitors of supernovae (SNe) is the early time light curve. The shape and duration of the rising light curve just after the explosion contain information about the initial shock breakout and cooling of the SN ejecta, as well as the distribution of circumstellar material near the SN, the density/composition profile of the progenitor star, and the properties of any companion stars (e.g., Piro, Chang, & Weinberg 2010; Kasen 2010; Rabinak & Waxman 2011; Piro & Morozova 2016; Kochanek 2019).

However, catching SN light curves significantly before peak brightness from the ground is difficult. Twelve SNe have been serendipitously observed within ∼3 days of the explosions (see Stritzinger et al. 2018, and references therein). The case of SN2011fe was particularly favorable since observations were obtained just 2–3 hours after the explosion (Nugent et al. 2011; Bloom et al. 2012). Ground-based transient surveys are reducing the delay from several days to 10–20 hours, using high-cadence observations from networks of telescopes (ASAS-SN, Shappee et al. 2014), wide-field instruments (ZTF, Bellm et al. 2019; ATLAS, Tonry et al. 2018e), or high-cadence studies of specific targets (1M2H, Coulter et al. 2017; DLT40, Valenti et al. 2017).

The *Kepler* spacecraft opened a new window on the early time light curves of SNe by continuously monitoring several hundred galaxies over the four years of its primary mission,

and more than 9000 galaxies in the *K2* Campaign 16 Supernova Experiment. These programs yielded light curves of six SNe from before the explosion through the early rise, including ASASSN-18bt, which has the highest precision of any SN light curve to date (Olling et al. 2015; Garnavich et al. 2016; Shappee et al. 2019; Dimitriadis et al. 2019).

The Transiting Exoplanet Survey Satellite (TESS, Ricker et al. 2015) has the potential to significantly expand the sample of early time SN light curves. TESS combines an ability to perform nearly continuous monitoring from a stable space-based platform over time intervals as long as one month to one year, with an extremely wide field-of-view (24×96 degrees). The continuous monitoring allows TESS to observe a SN at the moments just after the explosion, while the wide field-of-view drastically increases the probability of observing bright SNe. Despite the small apertures of its cameras, TESS can achieve a 3σ limiting magnitude in 8 hours of $\sim$20 mag, and thereby make useful photometric measurements of extragalactic transients.

In this letter, we present early time TESS light curves of the 18 Type Ia SNe listed in Table 1, which we use to constrain the explosion physics and the properties of possible companion stars. Nine of these SNe were discovered by ASAS-SN (Shappee et al. 2014), four by ATLAS (Tonry et al. 2018e), four by ZTF (Bellm et al. 2019), and one by *Gaia* (Gaia Collaboration et al. 2016). ASAS-SN recovered four of the SNe found by the other three projects, and has increased the cadence with which it observes the TESS fields in order to discover interesting transients that will benefit from continuous TESS data. This is an important point because TESS data are downloaded and released several weeks after the observations, but the transients must be identified earlier in order to obtain timely multi-wavelength observations and spectroscopy. One of these SNe, ASASSN-18tb, is discussed in more detail in Vallely et al. (2019).

In §2 we review the TESS observations and in §3 we describe our data reduction. In §4 we present our analysis techniques, and in §5 we compare our results to models of companion stars interacting with the SNe ejecta. Finally, in §6 we assess the impact that TESS will have on the sample of early time SNe light curves and summarize our conclusions. Throughout, we assume a consensus cosmology with $H_0 = 70$ km s^{-1}, $\Omega_m = 0.3$, and $\Omega_\Lambda = 0.7$. We correct for Galactic extinction estimated by Schlafly & Finkbeiner (2011) with a Cardelli, Clayton, & Mathis (1989) extinction law and $R_V = 3.1$.

2. OBSERVATIONS

TESS (Ricker et al. 2015) began its survey of the southern ecliptic hemisphere in July of 2018. Every 27 days, TESS slews 14 degrees eastward of the antisolar direction while keeping the center of the field of Camera 4 fixed at the ecliptic pole[1]. During each 27 day pointing, the fields of the four wide-field cameras ($24^\circ \times 24^\circ$ per camera) define a "sector" that covers approximately 1/18th of the sky stretching from 6° from the ecliptic plane to 12° beyond the ecliptic pole. The first six sectors of TESS observations swept over nearly a quarter of the sky from 2018 July 25 through 2019 January 06. In each sector, full-frame images (FFIs) are continuously collected at a 30-minute cadence. Cosmic rays are corrected on-board by the flight software, resulting in an effective exposure time of 1440 seconds per FFI. TESS observes in a single broad-band filter, ranging from about 600–1000 nm with an effective wavelength of 800 nm.

Several events occurred in the first six sectors that affect the quality of the data, as documented in the TESS data release notes[2]. In Sector 3, time was taken to perform additional tests of the attitude control system. In Sector 4, the cameras were turned off for several days in response to an instrument data-system anomaly, which led to a significant change in the thermal state of the instrument. Finally, at the end of Sector 5, a high level of scattered light from the Earth affected the spacecraft pointing. In our analyses, we ignore all data from these suspect epochs.

3. DATA REDUCTION

We extracted light curves using our custom TESS Transient Pipeline. The pipeline interfaces directly with the Transient Name Server[3] (TNS) to produce differential light curves of reported astrophysical transients that land in the TESS field-of-view. The details of the pipeline will be provided in a forthcoming contribution, but a brief description is provided here.

The data reduction consists of two steps. First, we process TESS FFIs from each sector using the difference imaging technique described by Alard & Lupton (1998) and Alard (2000). Second, we make photometric measurements for each transient source at pixel coordinates in the difference images using celestial coordinates from TNS and a model of the instrument geometry[4]. Differential flux measurements are calculated by fitting a model of the instrument pixel-response function (PRF) to the appropriate pixels in the difference images.

In total, there were 42 SNe brighter than 20th magnitude at discovery reported to TNS and observed by TESS in the first six sectors. Of these, 34 were Type Ia, which we focus on here. Eighteen of the SNeIa unambiguously show a ris-

[1] For the first year of the mission the fields lie in the southern ecliptic hemisphere, and, in the second year, will lie in the northern ecliptic hemisphere.

[2] https://archive.stsci.edu/tess/tess_drn.html

[3] https://wis-tns.weizmann.ac.il/

[4] An open-source, pure-python implementation of the focal plane geometry model is available at https://github.com/christopherburke/tess-point

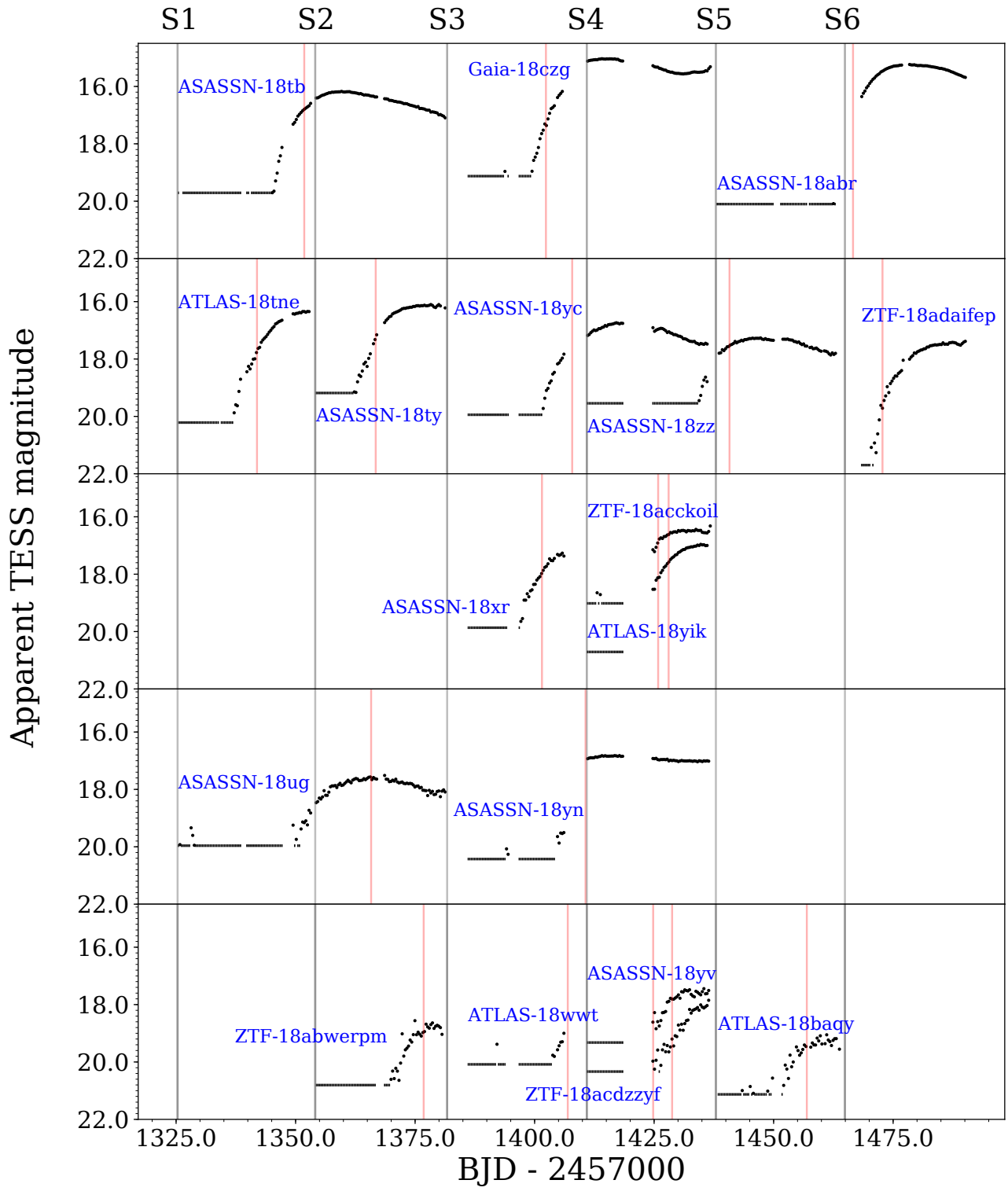

Figure 1. Light curves of the 18 Type Ia SNe observed in the first six sectors of TESS data. The data are binned to 8 hours and flux-calibrated as described in §3. Pre-explosion magnitudes are 3σ upper limits. The SNe are roughly ordered from top to bottom by apparent magnitude at peak. The vertical red lines mark the times of discovery.

Table 1. Properties of the Supernova Sample

Name		$T_{\rm peak}$	ΔT	M_T	νL_ν	Redshift	$E(B-V)$	Discovery	Classification
		(mag)	(mag)	(mag)	(erg s^{-1})		(mag)		
ATLAS-18tne	(SN2018exc)	16.34	3.87	-20.71 ± 0.14	2.92×10^{47}	0.0570	0.034	Tonry et al. (2018a)	Stein et al. (2018)
ASASSN-18tb	(SN2018fhw)	16.02	3.69	-18.34 ± 0.44	3.03×10^{46}	0.0170	0.027	Brimacombe et al. (2018a)	Eweis et al. (2018), Kollmeier et al. (2019), Vallely et al. (2019)
ASASSN-18ty	(SN2018fub)	16.13	3.06	-19.38 ± 0.26	8.30×10^{46}	0.0288	0.011	Brimacombe et al. (2018b)	Strader (2018)
ASASSN-18ug	(SN2018fvi)	17.54	2.43	-18.74 ± 0.20	4.63×10^{46}	0.0404	0.025	Brimacombe et al. (2018c)	Strader (2018)
ZTF-18abwerpm	(SN2018grv)	18.78	2.03	-18.74 ± 0.11	4.88×10^{46}	0.0700	0.032	Fremling (2018a)	Fremling et al. (2018d)
ASASSN-18xr	(SN2018hgc)	17.26	2.60	-19.57 ± 0.15	1.02×10^{47}	0.0520	0.026	Brimacombe et al. (2018d)	Dimitriadis et al. (2018)
Gaia-18czg	(SN2018hib)	15.04	4.08	-19.21 ± 0.45	6.89×10^{46}	0.0163	0.019	Delgado et al. (2018)	Reguitti et al. (2018)
ATLAS-18wwt	(SN2018hka)	–	–	–	–	0.0370	0.029	Tonry et al. (2018b)	Fremling et al. (2018a)
ASASSN-18yc	(SN2018hkx)	16.72	3.22	-18.48 ± 0.30	3.54×10^{46}	0.0250	0.036	Nicholls et al. (2018)	Jha et al. (2018)
ASASSN-18yn	(SN2018hpu)	17.81	2.62	-19.47 ± 0.39	1.05×10^{47}	0.0660	0.013	Brimacombe et al. (2018e)	Hiramatsu et al. (2018a)
ASASSN-18yv	(SN2018hss)	17.55	1.78	-18.85 ± 0.18	5.27×10^{46}	0.0430	0.009	Brimacombe et al. (2018f)	Hiramatsu et al. (2018b)
ZTF-18acckoil	(SN2018hyy)	16.47	2.55	-19.06 ± 0.25	6.10×10^{46}	0.0290	0.025	Fremling (2018b)	Fremling et al. (2018b)
ATLAS-18yik	(SN2018hzh)	16.99	3.72	-18.95 ± 0.21	5.71×10^{46}	0.0350	0.005	Tonry et al. (2018c)	Bose et al. (2018)
ZTF-18acdzzyf	(SN2018ieu)	17.96	2.38	-18.31 ± 0.19	3.16×10^{46}	0.0405	0.019	Nordin et al. (2018a)	Fremling et al. (2018c)
ASASSN-18zz	(SN2018ioa)	17.17	2.38	-19.19 ± 0.26	6.80×10^{46}	0.0412	0.021	Brimacombe et al. (2018g)	Bose et al. (2018)
ATLAS-18baqy	(SN2018jnd)	19.24	1.89	-18.87 ± 0.09	5.49×10^{46}	0.0900	0.088	Tonry et al. (2018d)	Fremling et al. (2018e)
ASASSN-18abr	(SN2018jwi)	15.25	4.85	-19.12 ± 0.43	6.04×10^{46}	0.0170	0.064	Cacella et al. (2018)	Pursiainen et al. (2018)
ZTF-18adaifep	(SN2018koy)	17.45	4.25	-18.29 ± 0.24	2.72×10^{46}	0.0310	0.122	Nordin et al. (2018b)	Pineda et al. (2019)

NOTE—Absolute magnitudes M_T are calculated from the classification redshift and corrected for Galactic extinction using the Cardelli et al. (1989) extinction law with $R_V = 3.1$ and the given value of $E(B-V)$ from Schlafly & Finkbeiner (2011). We assume an error of 1000 km s^{-1} on the redshifts. No K correction is applied. Apparent peak magnitudes $T_{\rm peak}$ are observed values, uncorrected for Galactic extinction.

ing light curve after a flat time interval where the SNe flux is either zero or well below the TESS detection limit. For 11 other SNe, we can clearly detect a SNe signal, but pre-explosion TESS observations were not obtained. For the remaining five sources, we did not detect any SN signal. These cases are either very faint (>18 mag at discovery) or are close to bright stars that contaminate the SN signals in the difference images (see §3.1 below).

For the 18 Type Ia SNe with pre-explosion observations, we flux-calibrated the light curves by assuming that any pre-explosion flux was negligible. If the SNe was observed across two sectors, we solved for a sector-to-sector offset that best aligns the first 0.5 days of the second sector to an extrapolated rising power law fit of the light curve in the first sector (see §4). We then converted the units of our light curves from electrons per second (r_e) to TESS magnitudes (T) with $T = -2.5\log_{10}(r_e) + Z_T$, where Z_T is the TESS image zero-point. The average image zero-point across the four cameras is $Z_T = 20.44 \pm 0.05$ mag, measured during commissioning from observations of bright isolated stars (Vanderspek et al. 2018). We define the limiting magnitude $T_{\rm limit}$ by binning the light curves of each source to 8 hours, measuring the root-mean-square scatter σ of the values in the pre-explosion 8-hour bins, and setting $T_{\rm limit} = -2.5\log_{10}(3\sigma) + 20.44$. The limiting magnitudes range from 19.02 to 21.76, depending on the quality of the subtractions, the proximity of the SNe to bright stars, and time-variable structure in the image backgrounds. We also rescaled the default pipeline uncertainties, which only account for photon noise in the images, to match the observed pre-explosion root-mean-square scatter. The rescaling factor is typically between 2.0 and 3.0.

Figure 1 shows the final flux-calibrated light curves binned to 8 hours for the 18 SNe listed in Table 1, and Table 2 gives the light curves. Of the physical properties given in Table 1, the peak magnitude $T_{\rm peak}$ and the difference between the peak and limiting magnitudes $\Delta T = T_{\rm limit} - T_{\rm peak}$ are particularly important, since these quantities determine the signal-to-noise ratio and dynamic range of the early time light curves. Absolute magnitudes M_T were determined based on the redshifts reported in the classification references. We assumed uncertainties on the redshifts of 1000 km s^{-1}.

For six objects (ASASSN-18tb, ASASSN-18ug, Gaia-18czg, ASASSN-18yc, ASASSN-18zz, and ASASSN-18abr), we were also able to measure Δm_{15} (the increase in the magnitude 15 days after peak, Phillips 1993) from the late time light curves and thereby estimate the absolute magnitudes independently of the redshifts. To determine Δm_{15}, we used SNooPy (Burns et al. 2011) to fit i-band Type Ia SN templates to the TESS light curves. The templates were adapted to the TESS instrument response neglecting any internal host-galaxy extinction, and converting i-band magnitudes to TESS magnitudes by subtracting 0.49 mag, based on synthetic photometry of the Type Ia spectral energy distribution (SED) templates of Hsiao et al. 2007. The difference between the absolute magnitude determined using the redshift-based distances and that determined using Δm_{15} ranges from –0.87 to 0.96 mag. The mean difference is 0.1 mag in the sense that the redshift-based distances are larger than the Δm_{15} distances. The systematic errors in the redshift-based distances of local SNe primarily arise from the difficulty of removing any blue-shift due to the SN expansion from the host's cosmological redshift. Since we do not have late-time light curves for all of the 18 SNe and therefore do not have a complete set of Δm_{15} estimates, we use the redshift-based distances for consistency. Future work may leverage additional multiwavelength observations of these SNe to tightly constrain Δm_{15} and provide more precise distances.

Table 2. TESS Supernova Light Curves

Name	BJD−2457000.0 (days)	Flux (e s^{-1})	Flag
ATLAS−18tne	1325.315264	−0.82 ± 1.52	B
ATLAS−18tne	1325.336095	3.16 ± 1.54	B
ATLAS−18tne	1325.356927	1.67 ± 1.54	B
...	...	...	...

NOTE—Light curves for all 18 SNe are presented in a single table, available upon request. The Flag column indicates epochs that we suspect suffer from large systematic errors, based on visual inspection of the images and correlations with ancilliary data. The adopted Flag indicators are: A = Asteroid moving through photometric aperture; B = Background estimate suspect (scattered light and/or glints, see §3.1); P = Pointing offset or change; T = Temperature of camera lens barrel may have an effect. A machine readable version of this table is available in the online version of this article.

3.1. *TESS Systematic Errors*

Pointing jitter and scattered light/glints are the two main causes of systematic errors in the TESS light curves. These issues are described in detail in Vanderspek et al. (2018) and the individual data release notes for each sector. In order to mitigate the impact of jitter and scattered light on our results, we removed from further analysis any data where the effects are particularly notable.

For pointing jitter, we binned the mission-supplied pointing offsets in quaternion form to the 30-minute intervals of each FFI, and performed three rounds of 5σ clipping using both the binned quaternions and the dispersion within each bin. This procedure removes images with large pointing errors or poor pointing stability.

For scattered light and glints, we performed three rounds of 5σ clipping on the local background estimates. This procedure removes outliers in the distribution of background estimates, and catches most rapidly moving glints. However, sigma-clipping tends not to perform well around the times when the Earth or Moon rise above or set below the spacecraft sunshade. We therefore flagged additional images based on the background-estimate time series and visual inspection of the difference images. The problem is most acute at the ends of Sector 4 and Sector 5, for which we manually excluded data from the light curves of ASASSN-18zz (Sector 4, BJD − 2457000 = 1436.020 to 1436.812) and ASASSN-18abr (Sector 5, BJD − 2457000 = 1463.605 to 1464.251). The TESS mission also excluded these time intervals from their transiting planet search because of strong and rapidly changing background features. ASASSN-18zz and ASASSN-18abr are the only sources for which these features affect the early time light curves—other sources are clearly affected at these times, but it does not impact our analysis of the initial rise and so the data are shown for completeness. We also found some evidence of residual background errors in the light curves from Sectors 1 and 2 of ATLAS-18tne, ASASSN-18tb, and ASASSN-18ty based on visual inspection. In these cases, there is no clear justification for excluding the data, but it is likely that the early time light curves are affected. We therefore include the data in further analysis, but regard the results with caution.

The final class of systematic errors occurs when a bright star lands near a SN in the TESS images. Imperfect residuals in a difference image can then contaminate the photometric aperture. Given the large plate scale ($21\farcs19$ per pixel), this is a common effect: ASASSN-18tb, ASASSN-18ug, Gaia-18czg, ASASSN-18yv, ZTF-18acckoil, and ASASSN-18zz are all affected. In most cases, there is a very bright star within 2 or 3 pixels with obvious residuals in the difference images. We were able to remove the main effects of these residuals by (1) extracting light curves of the contaminating stars, (2) smoothing with a median filter, and (3) fitting a shift and scale factor to the affected parts of the SNe light curves. We then subtract the scaled and smoothed star light curve from the SN light curve. A detailed discussion of this procedure is described by Vallely et al. (2019, see their Figures 3 and 5) for the case of ASASSN-18tb. For ASASSN-18ug and ASASSN-18yv, a bright star is extremely close to the SN in the image, and although this method improves the light curves, it is likely that the results are still subject to strong systematic errors. A more sophisticated detrending algorithm might help with this problem in the future.

4. ANALYSIS

For light curves with high dynamic range between the initial detection and the peak, it is possible to gain insight into the explosion physics and place limits on the size of any companions. We begin by parameterizing the light curves with a rising power law fit of the form

$$F(t) = H(t-t_0)A(t-t_0)^{\beta} + B \quad (1)$$

where t_0 is the time of the first detection, A, B and β are constants, and $H(t)$ is the Heaviside function. The parameter B accounts for any residual background flux at early times, and must be included to properly estimate the uncertainties in β. Following Olling et al. (2015), we only fit the light curves up to 40% of the peak flux. For ATLAS-18yik, the onset of the light curve rise is missing due to data gaps. A large portion of the early rise of ASASSN-18abr is also missing, although we detect the initial onset of its rise. For these cases, our fitting procedure is still able to constrain t_0 and β if we extrapolate the observed power law through the gaps. We estimate the uncertainties on fitted parameters with 1000 iterations of bootstrap resampling, and report the widths of the central 68% confidence intervals of the resulting parameter distributions.

We focus on the 8 SNe with $\Delta T > 3.0$ mag. Table 3 gives the best-fit values of t_0 and β from the rising power law fits. For reference, a fiducial "fireball" model, with a constant temperature photosphere expanding at a constant velocity (Riess et al. 1999), has a rising power law index of $\beta = 2.0$. Five of the eight SNe have $\beta > 1.6$ and are consistent with the fireball model at the 3σ level, although the best-fit index for one of the five (ATLAS-18tne) is much larger ($\beta = 3.46 \pm 0.56$). Of the remaining three SNeIa, two have indices $\beta \approx 1.0$ (ASASSN-18yc, ZTF-18adaifep), while the index for ATLAS-18yik is too uncertain to conclude that it is either low or high ($\beta = 0.67 \pm 0.99$). We do not find any correlation between the power law indices and $T_{\rm peak}$ or ΔT, so we do not attribute these results to observational effects such as signal-to-noise ratio or our fitting procedure. However, there are reasons to be skeptical of two of the fits. The light curve for the SN with the largest power law index, ATLAS-18tne, was obtained from an image region with a complicated background that may affect the fit. Meanwhile, the light curve of the SN with the smallest power law index, ATLAS-18yik, has a large gap around the onset of the rise in flux. For this SN, t_0 is determined by extrapolating from the power law slope observed at significantly later times, which may not reflect the properties of the rise at first light.

Even though the reduced χ^2 values are consistent with unity in all eight cases, we searched for remaining systematic errors by correlating the residuals with the binned pointing offset quaternions, the dispersion of the binned quaternions in the 30-minute FFI intervals, the local background estimates, and the lens barrel temperatures. We did not find significant correlations except for the local background, which is often slightly anti-correlated with the residuals. This sug-

Table 3. Powerlaw Fit Parameters

Name	t_0	β	dof	χ^2/dof	Error Floor	Dynamic Range
	(BJD−2457000)				(Fraction of Peak)	
ATLAS-18tne	1330.60 ± 1.59	3.46 ± 0.56	716	0.84 ± 0.05	0.05	20:1
ASASSN-18tb	1343.51 ± 0.67	1.69 ± 0.28	918	0.91 ± 0.05	0.06	16:1
ASASSN-18ty	1357.98 ± 1.04	2.71 ± 0.46	553	0.92 ± 0.06	0.10	10:1
Gaia-18czg	1397.52 ± 0.18	1.86 ± 0.07	712	1.18 ± 0.05	0.04	25:1
ASASSN-18yc	1400.61 ± 0.21	1.13 ± 0.10	731	0.95 ± 0.05	0.09	11:1
ATLAS-18yik	1423.52 ± 2.93	0.67 ± 0.99	407	0.87 ± 0.07	0.05	20:1
ASASSN-18abr	1461.26 ± 0.87	1.97 ± 0.60	337	1.22 ± 0.08	0.02	50:1
ZTF-18adaifep	1470.77 ± 0.59	1.03 ± 0.18	360	0.79 ± 0.07	0.03	33:1

NOTE—Uncertainties are the central 68% confidence intervals for fits to 1000 iterations of bootstrap resampling. The Error Floor column is calculated from the 5σ scatter of the early time light curve, after binning to 8 hours. Below these limits we cannot distinguish between real structure in the light curve and correlated systematic errors. Note that these limits are more conservative than would be inferred from ΔT in Table 1 alone. The Dynamic Range column is the inverse of the Error Floor column and is analogous to signal-to-noise ratio.

gests that the backgrounds are imperfectly removed by our image subtractions, local background estimates, and "glint" screening (see §3.1). In order to proceed, we define the error floor of a light curve as the scatter in the pre-explosion light curves binned to 8 hours, equal to the values of σ defined in §3. Residuals larger than five times this error floor we regard as significant; below this limit, we cannot distinguish between real structure in the light curves and correlated systematic errors. These 5σ uncertainty floors are listed in the second-to-last column of Table 3, in units of flux relative to the peak flux.

In an analysis of a large sample of ground based early time Type Ia SNe light curves, Firth et al. (2015) found a range of rising power law indices, with a mean value of $\beta = 2.44 \pm 0.13$. Our findings are consistent with their result, except that Firth et al. (2015) found only one object out of 18 to have a rising power law index significantly less than $\beta = 2.0$ (PTF-10accd). We find two such objects out of eight, ASASSN-18yc and ZTF-18adaifep. Departures from a simple fireball model have been seen in other objects, for example in SN2012fr, SN2013dy, SN2014J, iPTF16abc, DLT17u, and ASASSN-18bt (Contreras et al. 2018; Zheng et al. 2013, 2014; Siverd et al. 2015; Goobar et al. 2015; Miller et al. 2018; Hosseinzadeh et al. 2017; Shappee et al. 2019). These sources exhibited more nearly linear rises in the optical for a few days, followed by sharper rises with power law indices closer to 2. Contreras et al. (2018) show that this behavior in the light curve of SN2012fr is consistent with a moderately mixed initial nickel profile, as modeled by Piro & Morozova (2016). Shappee et al. (2019) find that the early light curve of ASASSN-18bt is also broadly consistent with the models of Piro & Morozova (2016), although the detailed distribution of ^{56}Ni is likely more complex. In our sample, the light curve of ASASSN-18yc could be consistent with this picture, although there is a 4-day gap in observations at the end of Sector 3 when the non-linear phase would be expected to begin. On the other hand, the behavior of ZTF-18adaifep is difficult to reconcile with the Piro & Morozova (2016) models. There is no strong evidence for an increase in the slope during the rise of this source; if anything, the slope may be diminishing after seven to ten days post-explosion.

Figure 2 shows the power law indices as a function of peak SN absolute magnitude, with the sources requiring extrapolation to t_0 flagged with open circles. Ignoring ATLAS-18yik, there is a hint of a correlation between peak absolute magnitude and rising power law index—the SNe with lower power law indices have absolute magnitudes greater than −18.5, putting them on the faint end of the distribution of Type Ia luminosities. For comparison, the results for the *Kepler* SNe (Olling et al. 2015; Shappee et al. 2019) are shown in blue and cyan (corrected from the *Kepler* to TESS bandpass based on the Hsiao et al. 2007 template SED). These sources, particularly KSN2011c and ASASSN-18bt, reduce the correlation. More SNe with clean data and robust fits are needed to determine if there is any real pattern.

5. COMPARISON TO COMPANION MODELS

Next, we compare the early time TESS light curves with the analytic models from Kasen (2010) that describe the interaction of the SN ejecta with a companion star. In these models, the ejected material from the SN forms a bow shock as it encounters the companion star, producing a flash of X-ray emission followed by a quick rise and then slow decay of thermal emission at UV/optical wavelengths. The observed light curve depends on the viewing angle of the observer, the separation of the primary and secondary (which sets the Roche lobe radius of the secondary), and the mass, velocity, and opacity of the SN ejecta. We adopt the fiducial model of

Table 4. TESS Light curves for Kasen (2010) models at 100 Mpc[a]

Time	50 $R_\odot$		25 $R_\odot$		10 $R_\odot$		5.0 $R_\odot$		1.0 $R_\odot$		0.5 $R_\odot$		0.1 $R_\odot$	
(days)	(e s^{-1})	(mag)	(e s^{-1})	(mag)	(e s^{-1})	(mag)	(e s^{-1})	(mag)	(e s^{-1})	(mag)	(e s^{-1})	(mag)	(e s^{-1})	(mag)
0.001023	0.006878	25.8464	0.005772	26.0367	0.004573	26.2895	0.003825	26.4835	0.002537	26.9293	0.002121	27.1239	0.001392	27.5807
0.022525	0.164560	22.3992	0.136899	22.5990	0.106924	22.8673	0.088239	23.0758	0.056138	23.5669	0.045806	23.7877	0.027846	24.3281
0.044027	0.322945	21.6672	0.267421	21.8720	0.207291	22.1485	0.169844	22.3649	0.105653	22.8803	0.085075	23.1155	0.049556	23.7023
...	...	...	...	...	...	...	...	...	...	...	...	...	...	...

NOTE—A machine readable version of this table is available in the online version of this article.

[a] In the local universe, the effects of time dilation and K corrections are negligible, and these light curves can be scaled based on luminosity distance alone.

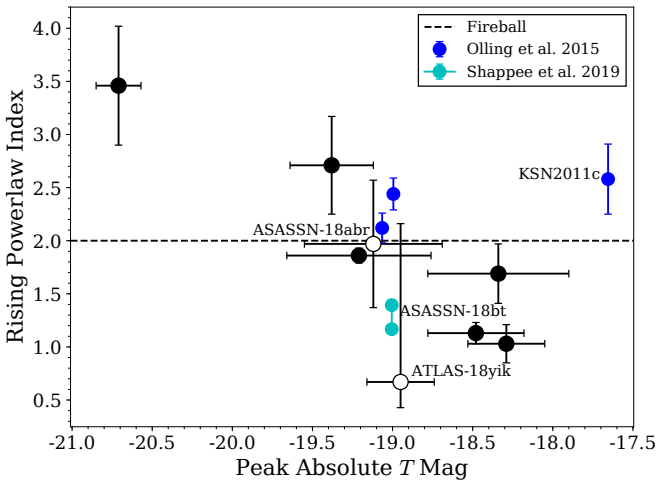

Figure 2. Rising power law index β as a function of absolute magnitude for the eight SNe observed by TESS with $\Delta T > 3.0$ mag (black points). Objects that require extrapolation to t_0 are shown with open circles. Ignoring theses sources, there is a hint in the TESS sample that flatter rises are associated with less luminous SNe. For comparison, results from *Kepler* (Olling et al. 2015; Shappee et al. 2019) are also shown (including both power law indices of the double component fit for ASASSN-18bt).

Table 5. Upper limits on Companion Parameters

Name	Separation	Radius
	(cm)	($R_\odot$)
ATLAS-18tne	5.1×10^{12}	25.1
ASASSN–18tb	3.5×10^{11}	1.7
ASASSN–18ty	2.9×10^{12}	14.2
Gaia-18czg	6.7×10^{11}	3.3
ASASSN–18yc	7.7×10^{11}	3.8
ZTF-18adaifep	1.9×10^{11}	1.0

Kasen (2010), with a viewing angle of 45°, an ejecta mass of 1.4 $M_\odot$, a velocity of 10^4 km s^{-1}, and an opacity of 0.2 cm^2 g^{-1}. A viewing angle of 0° corresponds to the explosion occurring directly behind the companion. We calculate light curves using the TESS wavelength-dependent response function, a blackbody spectrum with the temperature and photospheric radius defined by equations 24 and 25 of Kasen (2010) to represent the emission from the shock, and the appropriate luminosity distance for each source. Although our calculations incorporate the effects of redshift on the rest-frame SED and time dilation on the light curve, these effects are very small. For convenience, we provide the TESS light curve models at a fiducial distance of 100 Mpc in Table 4, and note that the flux can be rescaled with reasonable accuracy based on the luminosity distance alone. Finally, for each SN we consider increasing values of the separation, and therefore radius, of the secondary until the maximum flux exceeds the detection limit defined in §4. The relation between separation and Roche lobe radius is weakly mass dependent—we adopt primary/secondary masses of 1.4/1.0 $M_\odot$. This choice is unimportant at the level of detail presented here.

We restrict our analysis to the 6 SNe where continuous observations are available through a significant portion of the rising light curve. This removes ATLAS-18yik and ASASSN-18abr from further consideration. Table 5 shows the results for the remaining sources, and Figure 3 shows the power law fits, residuals, and model light curves for companions with the maximum allowable radius for each source. We are able to rule out giant companions with radii $\gtrsim 25$ $R_\odot$ in all six SNe, assuming the viewing angles are less than 45°. For four SNe, the data quality is superb and the limits reach down to 3.3–3.8 $R_\odot$ (Gaia-18czg and ASASSN-18yc), 1.7 $R_\odot$ (ASASSN-18tb), and 1.0 $R_\odot$ (ZTF-18adaifep). These upper limits do not take errors in t_0 and β into account, especially those in which t_0 occurs later than given by our fits. A thorough discussion of degeneracies between t_0, β, and the companion light curve is given in §4 of Shappee et al. (2019), but such a detailed analysis is beyond the scope of this work.

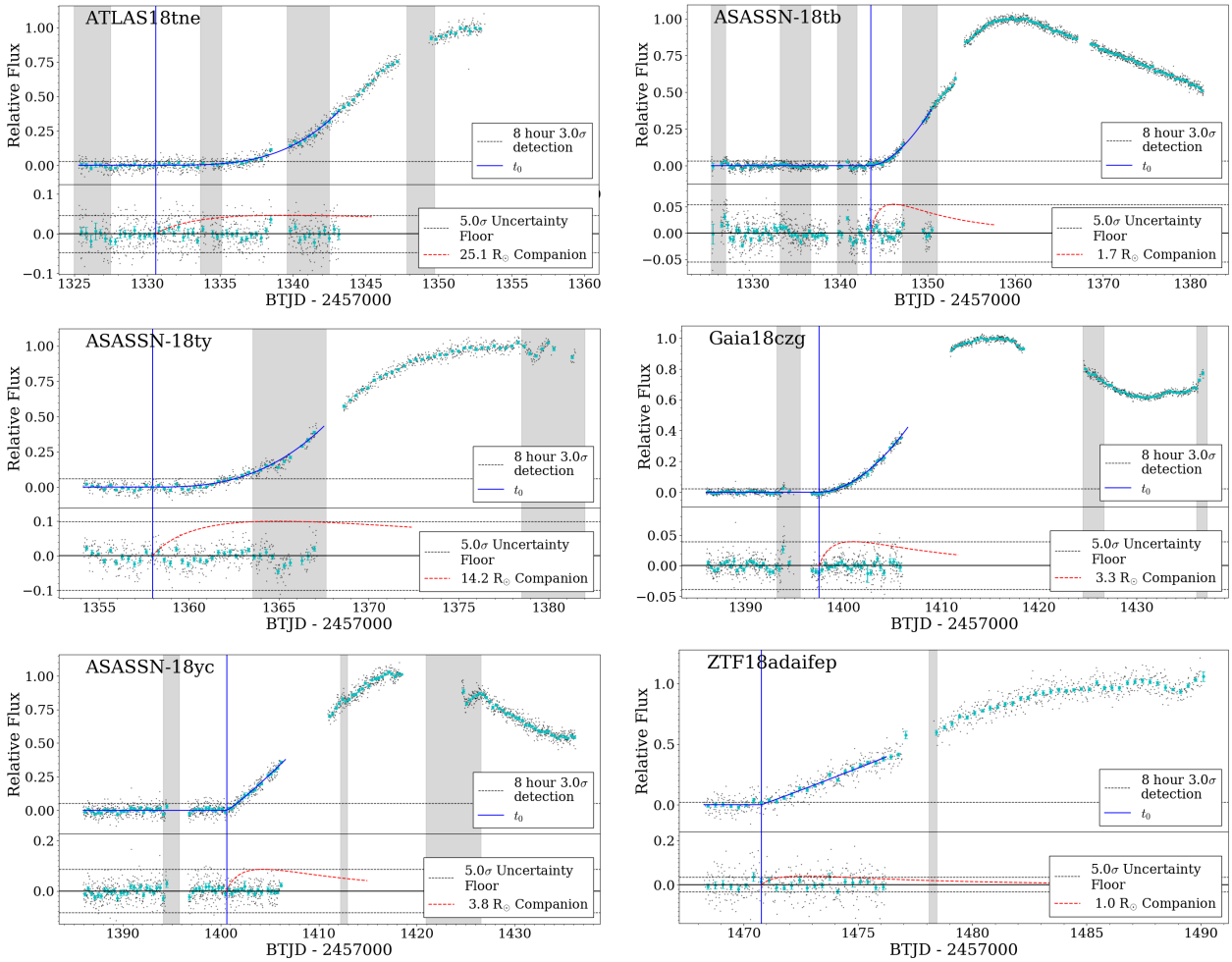

Figure 3. Power law fits, residuals, and light curves from the models of Kasen (2010, see §5) for the six SNe with high dynamic range and nearly continuous early time light curves. The black points are individual 30-minute FFI observations, and the cyan circles are binned to 8 hours. The shaded grey regions are periods flagged for complicated backgrounds (see §3.1). The top panels show the 3σ detection limits based on the dispersion of the pre-explosion flat baseline, while the bottom panels show the adopted 5σ systematic uncertainty floors (black dashed lines). The red dashed lines show the light curves produced by a companion with the maximum allowable radius based on the uncertainty floor, assuming a favorable viewing angle.

Errors in the adopted distances affect these results by changing the expected flux of the companion's signature. However the redshift-based distances in this sample tend to be larger than those estimated from Δm_{15}, and overestimated distances translate to more conservative upper limits. Three of these sources have Δm_{15} measurements, (ASASSN-18tb, Gaia-18czg, and ASASSN-18yc), and the differences in distance are equivalent to only 0.1 to 0.3 magnitudes. Using the Δm_{15} distances would improve the upper limits by 5–15% in these cases. Our calculation for ASASSN-18tb also agrees with that of Vallely et al. (2019), although the upper limit on the companion radius is higher because the redshift-based distance is slightly larger than their adopted distance.

Failure to detect companion signatures can always be attributed to unfavorable viewing angles where the shocked ejecta are behind the bulk of the optically thick SN ejecta. However, if no companion signature is found in a large sample of SN light curves, confidence intervals for limits on companion radii can be inferred by calculating the probability that all the SNe are viewed at unfavorable angles. For a uniform distribution of the cosine of the viewing angle, the probability that all six SNe are viewed at angles of more than 45° is 38% (no companions $\gtrsim 25$ R$_\odot$), while the probability for four SNe is 52% (no companions $\gtrsim 4.0$ R$_\odot$). To push these limits to the 5% or 1% level requires 18 or 28 SNe, respectively. A rigorous calculation would take into account the fact that detectable emission from a companion drops smoothly with inclination angle. However, given the number of bright SNe observed in 6 months, we expect TESS to capture about this many early time light curves during its two-year primary mission, with 16 ± 4 SNe sensitive to companions $\gtrsim 4.0$ R$_\odot$ and 28 ± 6 SNe sensitive to companions $\gtrsim 25$ R$_\odot$. In other

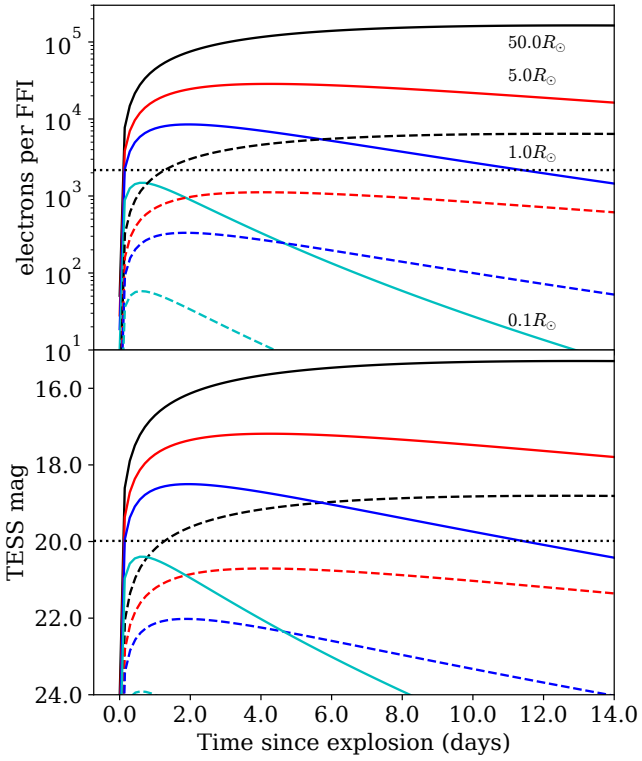

Figure 4. Model light curves from Kasen (2010), converted to electrons per single FFI and TESS magnitudes. We show light curves for R = 0.1, 1.0, 5.0, and 50 $R_\odot$ companions (from faintest to brightest) at either 50 Mpc ($z \approx 0.01$, solid curves) or 200 Mpc ($z \approx 0.05$, dashed curves). The horizontal line shows the typical 3σ detection limit for an 8 hour average of the FFIs. Within about ∼50 Mpc ($z \approx 0.01$), we expect to be able to detect emission from an 0.1–1.0 $R_\odot$ companion (see §6).

words, there is a 95% chance that TESS will detect emission from a SN Ia companion with radius > 4.0 $R_\odot$ and a 99% chance of detecting emission from a companion with radius > 25 $R_\odot$ by the end of the survey, assuming that such companions are common. A failure to detect any companion signature can be translated to stringent upper limits on single-degenerate scenarios.

6. FUTURE PROSPECTS AND CONCLUSION

This work shows the impact that TESS can have on transient and SN science. With its unique combination of continuous monitoring and survey area, TESS will be able to characterize the early time light curves of a large number of bright SNe in exquisite detail, and provide a sample of sources with which to constrain progenitor models.

With regard to the progenitor systems of Type Ia SNe, we have calculated the observable properties of companion signatures in order to identify the most promising SNe for future TESS analysis. Figure 3 shows the expected TESS light curves for the Kasen (2010) models. We also provide tabulations of the models for different companion radii at a fiducial distance of 100 Mpc in Table 4. For any SNe within ∼50 Mpc ($z \approx 0.01$) observed by TESS, we expect to be able to detect emission signatures from companions with radii between a 0.1–1 $R_\odot$. Such SNe would be quite bright, at least $T_{\rm peak} \approx 14.5$ mag. The constraints fall off with increasing distance, until little can be said about about any companions at distances greater than 200 Mpc ($z \approx 0.05$). These statements of course depends on the the adopted detection limit—since TESS improved its pointing stability in Sector 4, we have noticed a tendency for the detection limits to push fainter than the average value $\langle T_{\rm limit} \rangle \approx 20$ mag of the 18 SNe light curves presented here. It remains to be seen if this represents a global improvement in the 8 hour 3σ detection threshold, or if the limit is driven primarily by effects unique to each SN. However, we expect that TESS will provide strong constraints on giant and dwarf companions for any SNe brighter than 16–17 mag at peak. As discussed in §5, at the current rate TESS will observe enough Type Ia SNe in two years to constrain the radii of companion stars at greater than 95% confidence, resulting in a strong test of single-degenerate progenitor scenarios.

In summary, we have presented early time TESS light curves of 18 Type Ia SNe, eight of which are amenable to analysis of the early rise. We fit rising power law models and searched for signatures of any companions stars. Our main results are:

1. Most of our sources are consistent with fireball models with power law index $\beta \approx 2.0$. Two out of eight SNe have a much smaller rising power law index with $\beta \sim 1.0$. These two sources (ASASSN-18yc and ZTF-18adaifep) have well-determined light curves and small systematic uncertainty estimates.

2. We do not find obvious evidence for additional structure in the light curves or companion signatures. A key component of future work will be to improve the systematic error floors of the TESS light curves, in order to confidently identify any subtle structure in the early time light curves.

3. We place upper limits on the radii of any companion stars of $\lesssim 25$ $R_\odot$ for 6 SNe and $\lesssim 4.0$ $R_\odot$ for 4 SNe. These constraints assume a favorable viewing angle ($<45°$), which implies that the odds of non-detections in this sample, if such systems are actually commonplace, are 38% for companions $\gtrsim 25\,R_\odot$ and 52% for companions $\gtrsim 4\,R_\odot$. After its two year mission, TESS will likely observe enough SNe to either detect the signature of a companion star down to a few $R_\odot$, or set strong limits on the nature of companions of Type Ia SNe in the local universe.

Facility: TESS

Software: Matplotlib (Hunter 2007), Numpy (van der Walt et al. 2011), Scipy (Oliphant 2007), Astropy (Astropy Collaboration et al. 2018), limfit[5], pysynphot (STScI Development Team 2013), SNooPy (Burns et al. 2011), ISIS (Alard & Lupton 1998)

ACKNOWLEDGEMENTS

We thank Saul Rappaport for discussions about binary systems and mass transfer.

This paper includes data collected by the TESS mission, which are publicly available from the Mikulski Archive for Space Telescopes (MAST) and described in Jenkins et al. (2016). Funding for the TESS mission is provided by NASA's Science Mission directorate. This research has made use of NASA's Astrophysics Data System, as well as the NASA/IPAC Extragalactic Database (NED) which is operated by the Jet Propulsion Laboratory, California Institute of Technology, under contract with the National Aeronautics and Space Administration.

PJV is supported by the National Science Foundation Graduate Research Fellowship Program Under Grant No. DGE-1343012. KZS and CSK are supported by NSF grants AST-1515876, AST-1515927, and AST-1814440. CSK is also supported by a fellowship from the Radcliffe Institute for Advanced Studies at Harvard University. The work of AP was supported in part by the GINOP-2.3.2-15-2016-00033 project which is funded by the Hungarian National Research, Development and Innovation Fund together with the European Union. TD acknowledges support from MIT's Kavli Institute as a Kavli postdoctoral fellow.

REFERENCES

Alard, C. 2000, Astronomy and Astrophysics Supplement Series, 144, 363

Alard, C., & Lupton, R. H. 1998, ApJ, 503, 325

Astropy Collaboration, Price-Whelan, A. M., Sipőcz, B. M., et al. 2018, AJ, 156, 123

Bellm, E. C., Kulkarni, S. R., Graham, M. J., et al. 2019, Publications of the Astronomical Society of the Pacific, 131, 018002

Bloom, J. S., Kasen, D., Shen, K. J., et al. 2012, ApJ, 744, L17

Bose, S., Dong, S., Chen, P., et al. 2018, The Astronomer's Telegram, 12246, 1

Brimacombe, J., Vallely, P., Stanek, K. Z., et al. 2018a, The Astronomer's Telegram, 11976

—. 2018b, The Astronomer's Telegram, 12011

—. 2018c, The Astronomer's Telegram, 12015

—. 2018d, The Astronomer's Telegram, 12104

Brimacombe, J., Vallely, P., Shields, J., et al. 2018e, The Astronomer's Telegram, 12149

Brimacombe, J., Vallely, P., Stanek, K. Z., et al. 2018f, The Astronomer's Telegram, 12171

—. 2018g, The Astronomer's Telegram, 12228

Burns, C. R., Stritzinger, M., Phillips, M. M., et al. 2011, AJ, 141, 19

Cacella, P., Brimacombe, J., Vallely, P., et al. 2018, The Astronomer's Telegram, 12302

Cardelli, J. A., Clayton, G. C., & Mathis, J. S. 1989, ApJ, 345, 245

Contreras, C., Phillips, M. M., Burns, C. R., et al. 2018, ApJ, 859, 24

Coulter, D. A., Foley, R. J., Kilpatrick, C. D., et al. 2017, Science, 358, 1556

Delgado, A., Harrison, D., Hodgkin, S., et al. 2018, Transient Name Server Discovery Report, 1575

Dimitriadis, G., Hung, T., & Foley, R. J. 2018, Transient Name Server Classification Report, 1578

Dimitriadis, G., Foley, R. J., Rest, A., et al. 2019, ApJ, 870, L1

Eweis, Y., Jha, S. W., Camacho, Y., et al. 2018, The Astronomer's Telegram, 11980, 1

Firth, R. E., Sullivan, M., Gal-Yam, A., et al. 2015, MNRAS, 446, 3895

Fremling, C. 2018a, Transient Name Server Discovery Report, 1426

—. 2018b, Transient Name Server Discovery Report, 1718

Fremling, C., Dugas, A., & Sharma, Y. 2018a, Transient Name Server Classification Report, 1667

—. 2018b, Transient Name Server Classification Report, 1720

—. 2018c, Transient Name Server Classification Report, 1760

—. 2018d, Transient Name Server Classification Report, 1846

—. 2018e, Transient Name Server Classification Report, 1987

Gaia Collaboration, Prusti, T., de Bruijne, J. H. J., et al. 2016, A&A, 595, A1

Garnavich, P. M., Tucker, B. E., Rest, A., et al. 2016, ApJ, 820, 23

Goobar, A., Kromer, M., Siverd, R., et al. 2015, ApJ, 799, 106

Hiramatsu, D., Arcavi, I., Burke, J., et al. 2018a, Transient Name Server Classification Report, 1666

—. 2018b, Transient Name Server Classification Report, 1704

Hosseinzadeh, G., Sand, D. J., Valenti, S., et al. 2017, ApJ, 845, L11

Hsiao, E. Y., Conley, A., Howell, D. A., et al. 2007, ApJ, 663, 1187

Hunter, J. D. 2007, Computing in Science & Engineering, 9, 90

[5] https://lmfit.github.io/lmfit-py/index.html

Jenkins, J. M., Twicken, J. D., McCauliff, S., et al. 2016, in Society of Photo-Optical Instrumentation Engineers (SPIE) Conference Series, Vol. 9913, Software and Cyberinfrastructure for Astronomy IV, 99133E
Jha, S. W., Camacho-Neves, Y., Dai, M., et al. 2018, The Astronomer's Telegram, 12122, 1
Kasen, D. 2010, ApJ, 708, 1025
Kochanek, C. S. 2019, MNRAS, 483, 3762
Kollmeier, J. A., Chen, P., Dong, S., et al. 2019, arXiv e-prints, arXiv:1902.02251
Miller, A. A., Cao, Y., Piro, A. L., et al. 2018, ApJ, 852, 100
Nicholls, B., Vallely, P., Stanek, K. Z., et al. 2018, The Astronomer's Telegram, 12119
Nordin, J., Brinnel, V., Giomi, M., et al. 2018a, Transient Name Server Discovery Report, 1744
—. 2018b, Transient Name Server Discovery Report, 1975
Nugent, P. E., Sullivan, M., Cenko, S. B., et al. 2011, Nature, 480, 344
Oliphant, T. E. 2007, Computing in Science & Engineering, 9, 10
Olling, R. P., Mushotzky, R., Shaya, E. J., et al. 2015, Nature, 521, 332
Phillips, M. M. 1993, ApJ, 413, L105
Pineda, J., Razza, A., Gromadzki, M., & Yaron, O. 2019, Transient Name Server Classification Report, 8
Piro, A. L., Chang, P., & Weinberg, N. N. 2010, ApJ, 708, 598
Piro, A. L., & Morozova, V. S. 2016, ApJ, 826, 96
Pursiainen, M., Castro-segura, N., Smith, M., & Yaron, O. 2018, Transient Name Server Classification Report, 1936
Rabinak, I., & Waxman, E. 2011, ApJ, 728, 63
Reguitti, A., Stritzinger, M., Dong, S., & Bos, S. 2018, The Astronomer's Telegram, 12131, 1
Ricker, G. R., Winn, J. N., Vanderspek, R., et al. 2015, Journal of Astronomical Telescopes, Instruments, and Systems, 1, 014003
Riess, A. G., Filippenko, A. V., Li, W., et al. 1999, AJ, 118, 2675
Schlafly, E. F., & Finkbeiner, D. P. 2011, ApJ, 737, 103
Shappee, B. J., Prieto, J. L., Grupe, D., et al. 2014, ApJ, 788, 48
Shappee, B. J., Holoien, T. W. S., Drout, M. R., et al. 2019, ApJ, 870, 13
Siverd, R. J., Goobar, A., Stassun, K. G., & Pepper, J. 2015, ApJ, 799, 105
Stein, R., Callis, E., Kostrzewa-Rutkowska, Z., et al. 2018, The Astronomer's Telegram, 11947
Strader, J. 2018, Transient Name Server Classification Report, 1322
Stritzinger, M. D., Shappee, B. J., Piro, A. L., et al. 2018, ApJ, 864, L35
STScI Development Team. 2013, pysynphot: Synthetic photometry software package, Astrophysics Source Code Library, ascl:1303.023
Tonry, J., Stalder, B., Denneau, L., et al. 2018a, Transient Name Server Discovery Report, 1154
Tonry, J., Denneau, L., Heinze, A., et al. 2018b, Transient Name Server Discovery Report, 1582
—. 2018c, Transient Name Server Discovery Report, 1713
—. 2018d, Transient Name Server Discovery Report, 1887
Tonry, J. L., Denneau, L., Heinze, A. N., et al. 2018e, Publications of the Astronomical Society of the Pacific, 130, 064505
Valenti, S., David, Sand, J., et al. 2017, ApJ, 848, L24
Vallely, P. J., Fausnaugh, M., Jha, S. W., et al. 2019, arXiv e-prints, arXiv:1903.08665
van der Walt, S., Colbert, S. C., & Varoquaux, G. 2011, Computing in Science & Engineering, 13, 22
Vanderspek, R., Doty, J., Fausnaugh, M., et al. 2018, TESS Instrument Handbook, Tech. rep., Kavli Institute for Astrophysics and Space Science, Massachusetts Institute of Technology
Zheng, W., Silverman, J. M., Filippenko, A. V., et al. 2013, ApJ, 778, L15
Zheng, W., Shivvers, I., Filippenko, A. V., et al. 2014, ApJ, 783, L24